Scilight

Advanced Characterization

https://www.sciltp.com/journals/ac

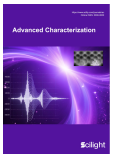

Article

Reversible Structure Formation in 4,4-Bipyridine—Fe 2D Metal-Organic Frameworks on Au(111)

Afra Gezmis [1], Simon Steinbach [1], Julien Steffen [2], Alisson Ceccatto [1], Isabela Tonon [3], Natalie Waleska-Wellnhofer [1], Abner de Siervo [3] and Hans-Peter Steinrück [1,*]

[1] Lehrstuhl für Physikalische Chemie II, Friedrich-Alexander-Universität Erlangen-Nürnberg, 91058 Erlangen, Germany
[2] Lehrstuhl für Theoretische Chemie, Friedrich-Alexander-Universität Erlangen-Nürnberg, 91058 Erlangen, Germany
[3] Institute of Physics Gleb Wataghin, University of Campinas, Campinas 13083-859, Brazil
* Correspondence: hans-peter.steinrueck@fau.de

How To Cite: Gezmis, A.; Steinbach, S.; Steffen, J.; et al. Reversible Structure Formation in 4,4-Bipyridine—Fe 2D Metal Organic Frameworks on Au(111). *Advanced Characterization* **2026**, *1*(1), 40–58.

Received: 27 March 2026
Revised: 7 May 2026
Accepted: 7 May 2026
Published: 25 May 2026

Abstract: Surface-confined metal–organic frameworks (2D MOFs) provide a versatile platform for studying low-dimensional coordination chemistry and tunable molecular architectures at atomic and molecular levels. Here, we investigate the self-assembly of 4,4-bipyridine and Fe on Au(111) and reveal a coverage-dependent phase behavior governed by metal–ligand coordination and surface availability. In the absence of Fe, 4,4-bipyridine forms a weakly substrate-coupled molecular network stabilized by intermolecular interactions. Fe coordination induces a sequence of distinct two-dimensional architectures, ranging from dense three-fold-coordinated tripod networks to open Kagome lattices composed of hexagonally arranged metal centers bridged by molecular linkers. Using scanning probe microscopy, low-energy electron diffraction, and density-functional theory calculations, we identify three thermodynamically stable phases with different coordination numbers, symmetries, and molecular densities. Transformations between these phases are reversible and controlled by the Fe-to-ligand ratio. These findings demonstrate how subtle control over coordination chemistry and surface coverage enables programmable structural transitions in two-dimensional metal–organic frameworks.

Keywords: 4,4-bipyridine; Fe; 2D MOF; structure transformation; STM; DFT

1. Introduction

Surface-confined or two-dimensional metal-organic frameworks (2D MOFs) have emerged as a distinct and rapidly expanding class of functional materials, combining the structural tunability of MOFs with the unique physicochemical properties associated with reduced dimensionality [1–3]. Composed of organic linkers coordinated to metal centers within an extended planar network, 2D MOFs exhibit high surface accessibility, anisotropic charge transport, and enhanced exposure of active sites, with a great potential for applications in sensing, catalysis, magnetism, gas storage and gas separation, energy harvesting, light emission, etc. [4–9]. The 2D MOFs are also a good platform for exploring fundamental physicochemical phenomena due to their versatility, adaptability, and geometry variety.

The structural diversity of 2D MOFs is governed by multiple factors, including the coordination geometry of the metal centers, the size, symmetry, and flexibility of the organic linkers [10], and the synthetic conditions under which the assembly occurs. Subtle variation in these parameters can lead to pronounced changes in framework morphology. In this context, the on-surface synthesis plays a key role in controlling the 2D MOF structure at the atomic and molecular levels. This strategy allows us to synthesize unique architectures inaccessible via other

preparation methods. Such control also enables phase transformation, breathing behavior, and reversible reorganization in response to external stimuli such as solvent, temperature, pressure, or guest molecules [11–13].

Despite extensive efforts to induce and control structural transformations in MOFs, most reported stimuli-response behaviors rely on external triggers or post-synthetic modifications [14,15]. In contrast, comparatively little attention has been paid to the role of reactant stoichiometry itself as a direct intrinsic control parameter for framework structure. Urgel et al., reported the formation of different structures, depending on the ratio of the molecule (para-quaterphenyl-dicarbonitrile) to the coordination center (Europium, Eu) on Au(111) [16]. The ratio between organic linkers and metal centers determines not only the local coordination environment, but also the long-range ordering of the resulting network. This effect is particularly pronounced in low-dimensional systems where small changes in bonding motifs can propagate across an entire layer. Lu et al. reported the break of crystalline order in a 2D MOF system by mixing two sizes of organic linkers [17]. Therefore, understanding how coordination interactions drive the self-assembly of low-dimensional materials is central to the rational design of surface-confined metal–organic frameworks.

In this work, by using scanning tunneling microscopy (STM), non-contact atomic force microscopy (nc-AFM), low-energy electron diffraction (LEED), and density functional theory (DFT) calculations (of free-standing adsorbate layers), we demonstrate that the interplay between molecular coverage, metal availability, and surface free-area governs a reversible phase transformation between distinct two-dimensional architectures formed by 4,4-bipyridine and Fe on Au(111). In the absence of metal coordination, 4,4-bipyridine assembles into a weakly substrate-coupled molecular network. At the same time, the introduction of Fe induces a hierarchy of coordination motifs ranging from dense three-fold-coordinated units to open Kagome lattices.

We identify three thermodynamically stable phases—non-coordinated molecular assemblies, compact tripod networks, and porous Kagome frameworks—that are selectively stabilized by the Fe-to-ligand ratio and molecular density. Transformations between these phases are fully reversible and proceed without chemical decomposition of the 4,4-bipyridine molecules, highlighting the dynamic nature of coordination bonding at surfaces. These findings establish coverage-controlled coordination as a powerful strategy for engineering adaptable 2D MOFs architectures with tunable density, symmetry, and high reversibility.

2. Results and Discussion

2.1. 4,4-Bipyridine Monolayer on Au(111)

We first studied the formation of a 4,4-bipyridine (4,4-bipy) monolayer deposited onto a freshly cleaned Au(111) surface at room temperature (RT). The saturated monolayer was achieved by evaporating 4,4-bipy with a home-built effusion cell. The evaporator was cooled with water but not heated, as the high vapor pressure of 4,4-bipy and the vacuum of the chamber were sufficient for the evaporation process (for details see Experimental Section). The sample rested at RT overnight to desorb the multilayer species and was cooled down to ~105 K for measurement.

In Figure 1a–c, the STM images of the saturated 4,4-bipy monolayer are depicted at different length scales, that is, scanning areas of (a) 50 × 50 nm^2; (b) 10 × 10 nm^2; and (c) 5 × 5 nm^2. We observe a mostly defect-free regular T-shaped arrangement of rectangular protrusions. Depending on the tip condition, the protrusions can also appear more oval, rather than rectangular. We assign each protrusion to one 4,4-bipy molecule; each molecule is surrounded by four neighboring molecules with perpendicular azimuthal orientations, forming the T-shape structure. Each N-termination of the aromatic ring faces the two H-atoms of a neighboring 4,4-bipy molecule (see overlay of scaled structural models in Figure 1c). These N-H interactions likely lead to the stabilization of the observed structure, as was previously proposed for similar systems [18–20]. This arrangement results in a quadratic unit cell (red square) with lattice vectors of a = b = 1.13 ± 0.08 nm length. The fast Fourier transformation (FFT) of the structure in Figure 1a is shown in Figure 1d, along with the unit cell in reciprocal space. We also investigated the saturated 4,4-bipy monolayer by non-contact atomic force microscopy (nc-AFM). The nc-AFM data show the same structure, but with lower image resolution. Thus, the corresponding images are only shown in Figure S1 in the Supplementary Materials (SM), along the STM data shown in Figure 1.

To obtain additional information, we studied the saturated 4,4-bipy monolayer also by low-energy electron diffraction (LEED). The corresponding diffraction pattern for a beam energy of 17 eV is shown in Figure 1e. The quite complex pattern is assigned to the coexistence of 6 symmetry-equivalent quadratic domains on the hexagonal Au(111) surface, rotated by ±4° (modulo 15°) relative to the three main substrate directions; the corresponding spots are schematically shown in Figure 1f in different colors for the different domains. Notably, domains with different orientations were found in STM as well. Exemplary STM images are shown in the SM (Figure S4). The reciprocal unit cell of one domain is exemplarily shown in red in Figure 1d to 1f. Notably, the (1,0) and symmetry-equivalent spots are missing, which is attributed to the two perpendicular mirror-glide planes of the adsorbate

structure (ignoring the substrate) [21,22]. By considering the six domains and the two glide planes we are able to reproduce the observed LEED pattern. In the SM, the LEED pattern at other beam energies (Figure S5) and a more detailed description of the analysis are provided (Figure S6), along with the LEED pattern of the clean Au(111) surface at higher electron beam energy (Figure S7).

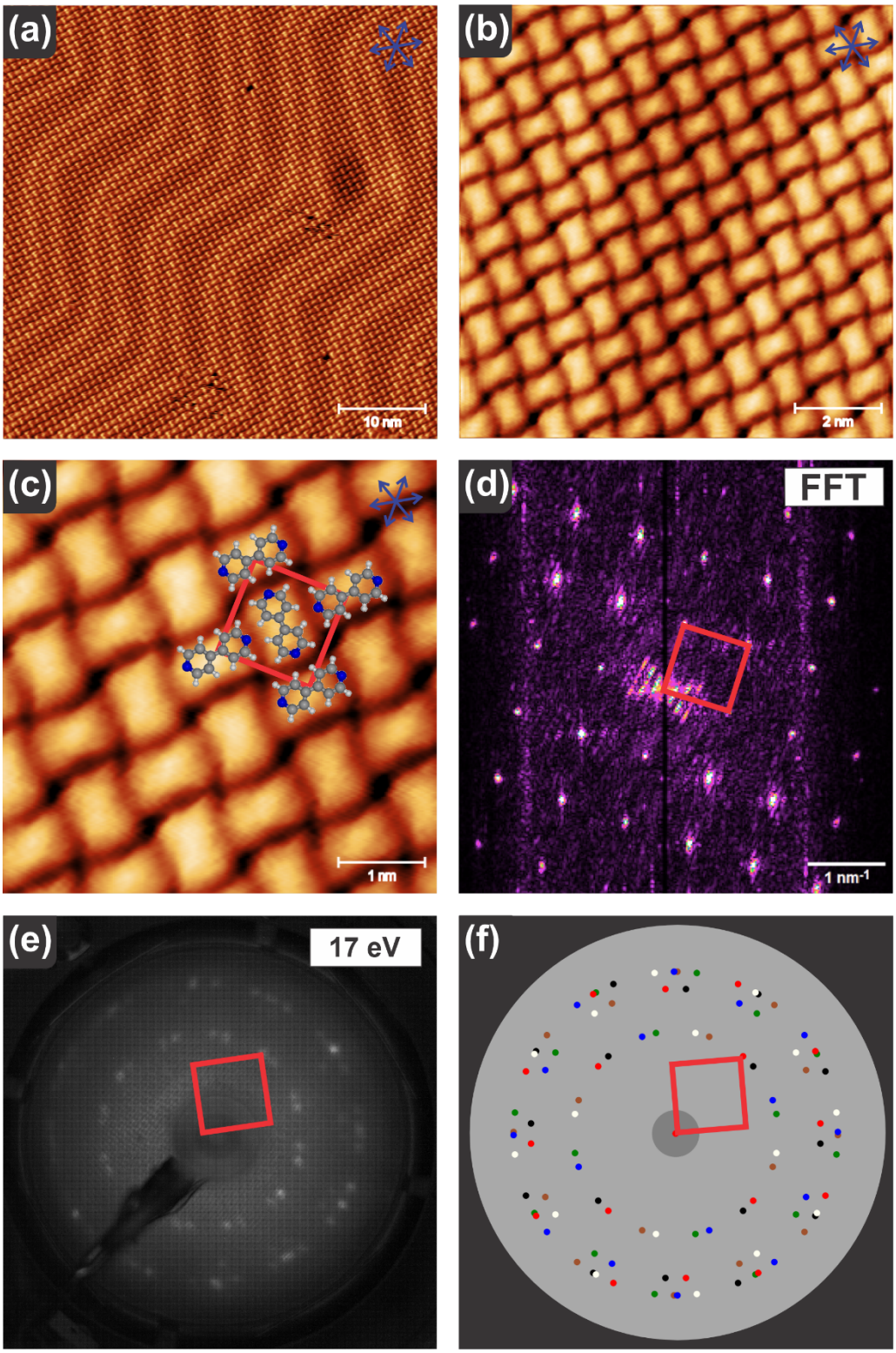

Figure 1. Saturated 4,4-bipy monolayer on Au(111), deposited at RT and cooled down to ~105 K for the measurements. (**a**–**c**) STM images with sizes of 50 nm × 50 nm, 10 nm × 10 nm, and 5 nm × 5 nm, respectively, displaying a well-ordered quadratic lattice with two perpendicularly oriented molecules in a T-shape arrangement per unit cell. The Au(111) substrate directions are indicated by blue arrows in the top right corners. In (**c**), the real space unit cell is shown as red square, and the scaled DFT-derived structure of a free-standing layer (see text) is superimposed. (**d**) FFT of the STM image. (**e**) LEED pattern measured with a beam energy of 17 eV. (**f**) Schematic

LEED pattern, with the diffraction spots of six symmetry equivalent domains (rotated relative to the substrate high symmetry directions by ±4°). In (**d**–**f**), the reciprocal unit cell of one domain is indicated as red square. The terminating N atoms of the pyridine ring are facing perpendicular to the H atoms at the 2 positions of both pyridine rings of a neighboring molecule, allowing the N-H interactions to stabilize the structure. For measurement parameters, please refer to the SM (Table S3).

A similar T-shape arrangement of 4,4-bipy, also with a quadratic unit cell, was already reported on Ag(111) by Dubois et al. by STM [23]. The structure was attributed to weak molecule-substrate interactions. Weak adsorbate-substrate interactions are also in line with the intact herringbone reconstruction of the Au(111) substrate in the presence of the 4,4-bipy monolayer, as evident from Figure 1a.

To understand the lateral interactions within the adsorbate layer, we performed DFT calculations for a free-standing 4,4-bipy layer, that is, neglecting the interaction with the substrate (for details see Supplementary Materials, SM). The square unit cell containing two molecules was obtained to have a size of 1.11 nm (see Figure S9c), in excellent agreement with experiment. This calculated structure is superimposed on the STM image in Figure 1c. Its formation energy is 0.92 eV per unit cell, that is, 0.46 eV per molecule (see Table S1 in the SM).

In order to study the thermal stability of the T-shape arrangement, we stepwise annealed the 4,4-bipy monolayer to 365, 412, and 450 K for 10 min, and after each annealing step, we performed STM measurements at 105 K. The corresponding STM images in Figure 2 show that the 4,4-bipy coverage decreases after each annealing step. After annealing to 450 K, no 4,4-bipy molecules were visible anymore. We therefore conclude that 4,4-bipy desorbs intact, as no signs of decomposition are observed. While volatile decomposition products cannot be fully excluded, we do not expect decomposition due to the weak interaction with the Au(111) substrate. The few small bright protrusions at the kinks of the Au(111) reconstruction are very likely due to small residual amounts of Fe on the surface, stemming from previous experiments, similar to those described below.

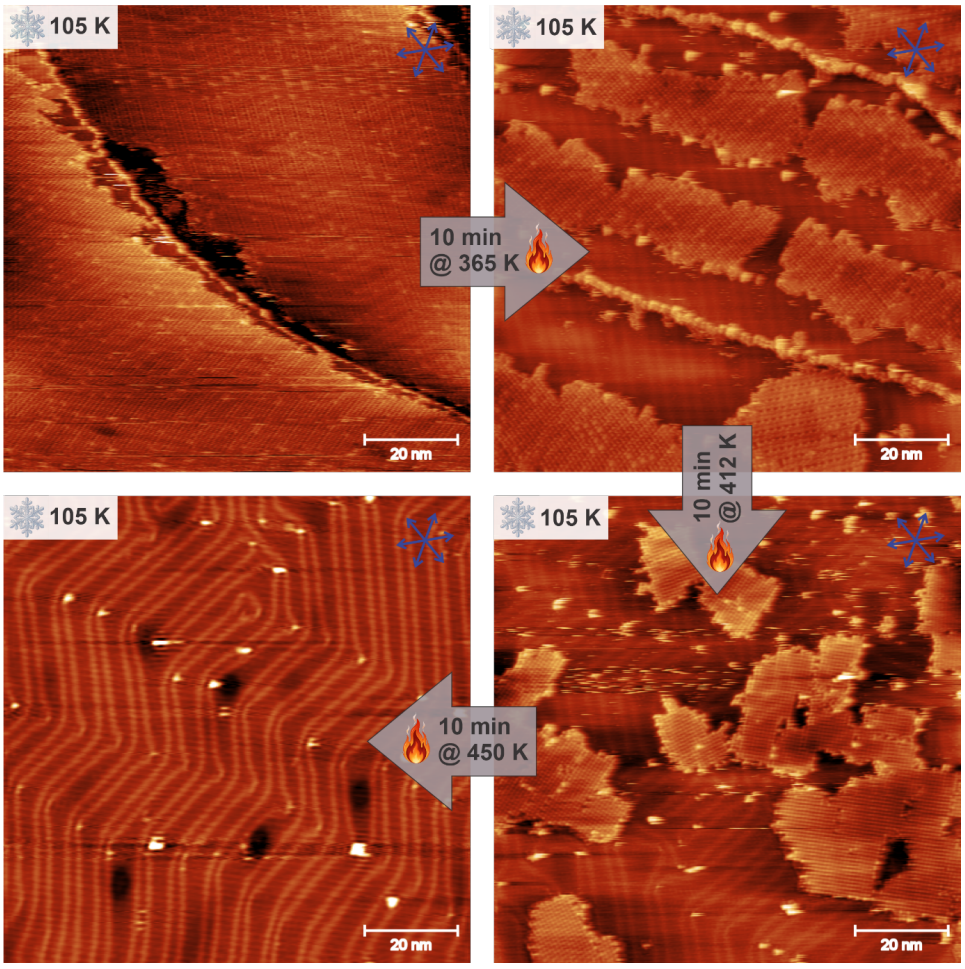

Figure 2. STM images (100 nm × 100 nm) of a saturated 4,4-bipy monolayer on Au(111). (**a**) deposited at RT; (**b**) after annealing to 365 K; (**c**) 412 K; and (**d**) 450 K for 10 min each. The sample was cooled down to ~105 K for measurement. The Au(111) substrate directions are indicated by blue arrows in the top right corners. For measurement parameters, please refer to the SM (Table S3).

2.2. Fe Deposition on Sub-Monolayer of 4,4-Bipyridine

In the next step, we deposited the same amount of Fe (~0.037 ML or ~0.51 atoms/nm^2) onto 4,4-bipy sub-monolayers with increasing coverages. Deposition was done with the Au(111) at RT, and STM images were measured at 105 K. At very low 4,4-bipy coverages (Figure 3a–c), we observe bright features at the kinks of the herringbone reconstruction (indicated as green circles in Figure 3b). We assign these features to the accumulation of Fe nanoparticles, which are known to form on Au(111) at low coverage and decorate the kinks [24]. The bright features in Figure 3a–c are connected by bright lines, which we assign to Fe-coordinated 4,4-bipy–Fe–4,4-bipy chains. Some of the chains consist of pore-like structures, as can be best seen in Figure 3c (bottom). While the chains appear to be stable, stripy features and partial broadening of the chains (see white arrows in Figure 3c) indicate mobile species, which could be partly induced by the STM tip. The formation of metal-coordinated chains at very low 4,4-bipy coverages has also been reported for 4,4-bipy on Cu(111), and has been assigned to metal coordination of the molecules by substrate Cu adatoms [23].

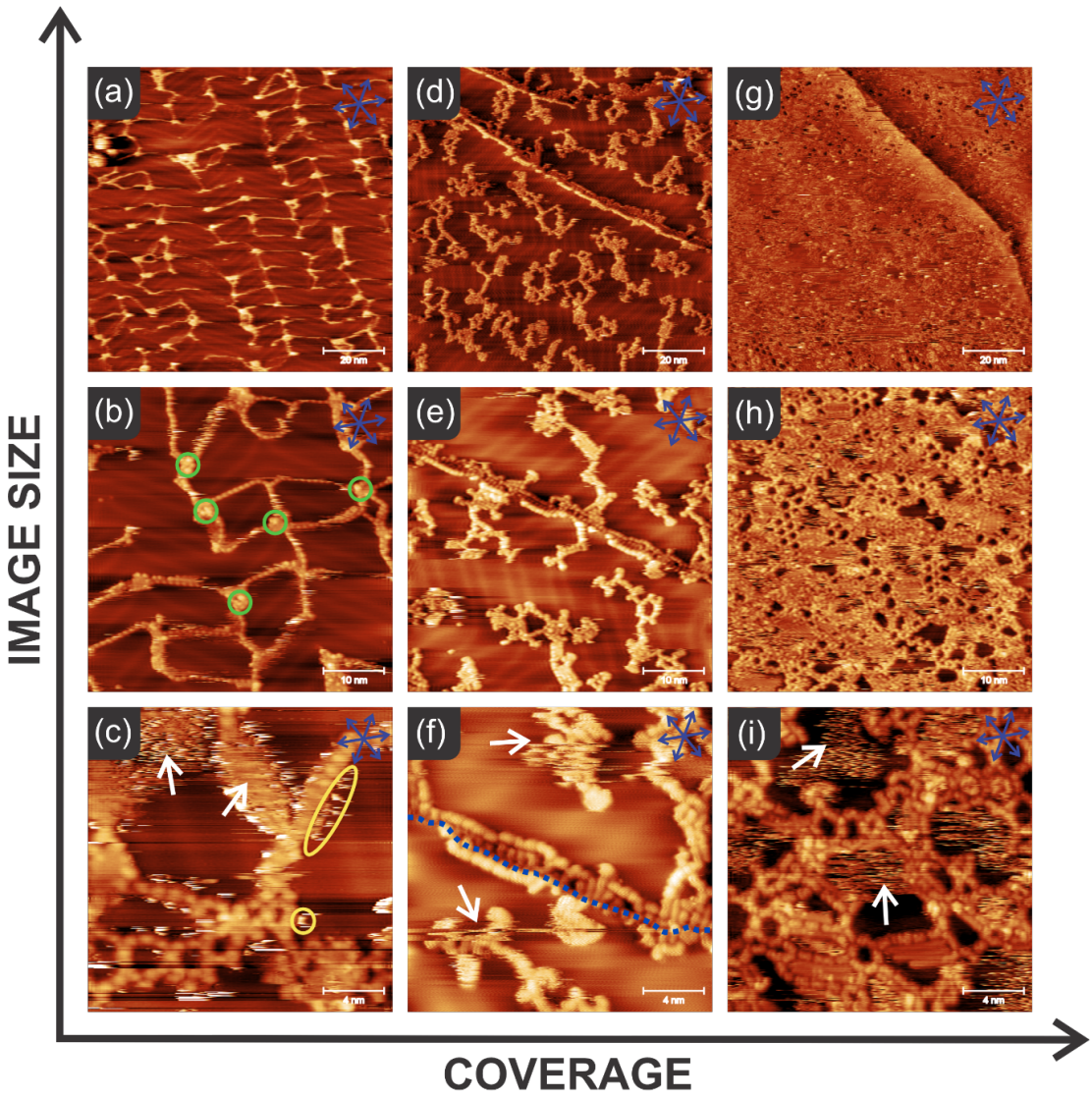

Figure 3. STM images after evaporating the same Fe dose of ~0.037 ML (equals ~0.51 Fe/nm^2) onto increasing 4,4-bipy sub-monolayer coverages on Au(111) (from left to right). The layers were prepared at RT and cooled down to ~105 K for measurement. STM images sizes decrease from top to bottom, from 100 nm × 100 nm, to 50 nm × 50 nm, and to 20 nm × 20 nm. The Au(111) substrate directions are indicated by blue arrows in the top right corners. (**a**–**c**) Very low coverage: the bright spots (green circles) are attributed to Fe nanoparticles at the kinks of the Au(111) herringbone reconstruction. Chains of oval protrusions (4,4-bipy–Fe–4,4-bipy chains) connect the nanoparticles, forming a line structure. (**d**–**f**) Low coverages: pore-like, mostly disordered structures; step edges are partly decorated (blue dashed line). (**g**–**i**) Intermediate coverage: pores of different shapes and sizes are observed. For all coverages, mobile structures and species are observed as indicated by stripy features or structure broadening (white arrows). For measurement parameters, please refer to the SM (Table S3).

For higher initial 4,4-bipy coverage, the bright features at the kinks of the herringbone structure as well as the connecting bright lines disappear and pore-like, but mostly disordered structures are observed in Figure 3d–f, which we attribute again to the Fe-coordination of 4,4-bipy. We attribute the disappearance of the bright features to the increased number of Fe-coordinated molecules at the increased 4,4-bipy coverage, which has used up all the Fe-islands at the kinks. The step edges (Figure 3f, blue dotted line) of the Au(111) substrate are decorated on both the lower and upper parts of the edge. The structures on the terrace do not show any regular order. Notably, resolving these structures in more detail has turned out to be difficult, due to the mobility of these structures, as deduced from the stripy features marked by white arrows in Figure 3f.

Upon further increasing the initial 4,4-bipy coverage, while keeping the amount of post-deposited Fe the same, we observe that a significant part of the surface is covered with small pore structures (Figure 3g–i). This becomes particularly evident in the small scale (zoom-in) image in Figure 3i, which shows that the surface is covered with small islands of Fe-coordinated 4,4-bipy pores of different sizes (white arrows); the stripy features again indicate the presence of mobile species.

The structures from Figure 3g–i, that is, the ones obtained with the largest 4,4-bipy coverage, were annealed to RT over 4 days to achieve a stable situation on the surface. In the corresponding STM images in Figure 4, we identified three different coordination motifs (indicated in different colors in the right column), which vary in the number of 4,4-bipy molecules coordinated to the Fe center. Notably, a coexistence of metal centers with different numbers of coordination partners have been reported also for other organic linkers, e.g., porphyrins [25].

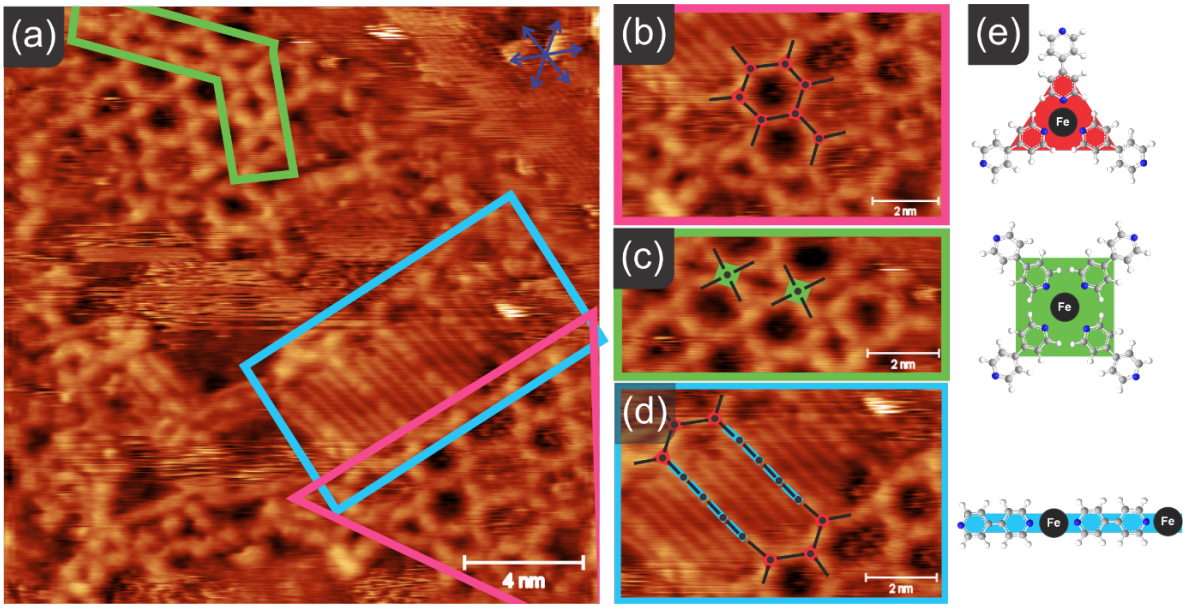

Figure 4. (**a**) STM image (20 nm × 20 nm) of an initial intermediate 4,4-bipy coverage after depositing Fe (~0.037 ML, equals ~0.51 Fe/nm^2) on Au(111) at RT (same preparation as for Figure 3g–i) and leaving the sample at RT for 4 days. Images were taken at ~105 K. The Au(111) substrate directions are indicated by blue arrows in the top right corner. Three different pore types are indicated: hexagonal (pink frame), diamond (green) and elongated (blue). Zoom-ins of these structures are shown on an enlarged scale in (**b**) hexagonal, (**c**) diamond, and (**d**) elongated. (**e**) Schematic illustrations of the three Fe coordination motifs observed: three-fold (red), four-fold (green), and linear (blue). These coordination motifs are indicated in the zoom-ins (**b**–**d**) showing how these motifs form the different pore types. For measurement parameters, please refer to the SM (Table S3).

These motifs alone or combined lead to three different structures formed by 4,4-bipy–Fe coordination. The three-fold coordination motif results in the formation of hexagonal or larger pores; a corresponding region with hexagonal pores is indicated by pink frames in Figure 4; notably, some of these pores appear to be filled, most likely with trapped 4,4-bipy molecules (or an unknown contamination). The four-fold coordination motif results in the formation of diamond-shaped pores, indicated in green in Figure 4. Finally, a two-fold coordination motif yields chains. When chains are capped with a three-fold coordinated motifs, one observes elongated pores; a corresponding region is indicated by a blue frame. These elongated pores have between 3 and 5 additional linear Fe–4,4-bipy units. The elongated pores are typically filled with three stripes of slightly dimmer appearance than the pore frame. Even for long pores, which are open on one side, this filling is observed. The distance between

these lines in the STM images is ~0.45 nm. We tentatively assign these lines to partially mobile excess 4,4-bipy molecules trapped in the the elongated pores.

In order to support this assumption, we performed DFT calculations for a free-standing elongated pore with three additional linear Fe–4,4-bipy units (see Figures S10 and S11 in the SM). The pore proved to be very stable with a formation energy of 2.89 eV per molecule. Adding of three or twelve 4,4-bipy molecules to the elongated pore leads indeed to a stabilization of these molecules by 0.53 and 0.43 eV per molecule, respectively, supporting our assignment (for details see SM).

2.3. Fe Deposition on a Saturated Monolayer of 4,4-Bipyridine

In the next experiment, we deposited ~0.037 ML of Fe (~0.51 atoms/nm^2) onto a full monolayer of 4,4-bipy on Au(111) at RT. The amount of deposited Fe was determined from the tripod structure described below (and the absence of additional islands of excess Fe). In subsequent STM at 105 K, we observe a new structure, which homogeneously covers the entire surface; see Figure 5a (and Figure S2 in the SM for corresponding nc-AFM images). It consists of triangular protrusions, which we denote as tripods, arranged in a regular pattern. We propose that each tripod is a three-fold-coordinated Fe center (reddish dot) connected to three 4,4-bipy molecules via one of the terminal N-atoms of the pyridine rings. The three-fold bonding motif of the Fe center is the same as observed above for the pore structure in Figure 4b. Closer inspection of Figure 5b reveals the coexistence of long-range ordered domains, in which the tripods have different orientation (white arrows); a corresponding domain boundary is exemplarily indicated as semitransparent green line. The orientation of the tripods is shown by yellow tripod bars for both domains. The 4,4-bipy arms of each tripod do not point exactly at the Fe center of the neigboring tripod, but are rotated by 12–15°. The resulting unit cell, shown in red in Figure 5c is hexagonal (or close to hexagonal), with lattice vectors of an equal length of 1.50 ± 0.15 nm and an enclosed angle of g = 60° ± 8°. The corresponding FFT image with the unit cell in reciprocal space is shown in Figure 5d. We also studied this structure by LEED. The corresponding diffraction pattern with a beam energy of 16 eV in Figure 5e shows a hexagonal pattern, which is in line with the FFT image; in Figure 5f the corresponding schematic pattern is shown. The reciprocal unit cell is shown in red in Figure 5d–f.

To understand the energetics of the tripods and their lateral interactions, we performed DFT calculations of a free-standing flat tripod structure with a hexagonal lattice (Figure S9b in the SM), that is, neglecting the interaction with the substrate, which is a crude estimation (for details see Supplementary Materials, SM). Nevertheless, the resulting lattice constant of 1.51 nm, with an angle of 60°, agrees very well with the value of 1.50 ± 0.15 nm determined from STM. The formation energy of the flat tripod (three 4,4-bipyridine and one Fe atom) in the gas phase is 3.76 eV per unit cell, and the formation energy of the unit cell is 0.63 eV, yielding an total formation energy of 1.46 eV per molecule, indicating a significant increase in thermodynamical stability as compared to the T-shape structure, due to the coordination to the Fe center (see Table S1 in the SM).

The calculated structure is superimposed on the STM image in Figure 5c. Comparsion of experiment and calculation reveals that in the STM images the 4,4-bipy molecules do not point exactly to the Fe atom of the neighboring tripod, but are rotated by 12–15°, as compared to a rotation angle of 0° in the calculation. We thus performed calculations for different rotation angles. It turns out that the calculated structures with rotated tripods are energetically not favored. We attribute this difference to the planarized structure of the tripod and the mentioned neglection of the substrate in the calculation. However, including the substrate would be computationally extremely demanding and is out of the scope of the present study.

In the next set of experiments, we subsequently added Fe at lower doses than in the previous experiment onto a full 4,4-bipy monolayer in order to study the transformation from the T-shape 4,4-bipy structure to the tripods (Figure 6). For each Fe deposition step, the sample was heated to RT. Depositing 10% of the amount required for the full tripod layer in Figure 5 leaves the T-shape structure mostly still intact; see Figure 6a. The incorporation of Fe into the structure is indicated by defects (white arrows in Figure 6b), where the structure starts breaking apart. Small indications of tripod formation can be seen in the defect sites (yellow tripod bars in Figure 6b,c).

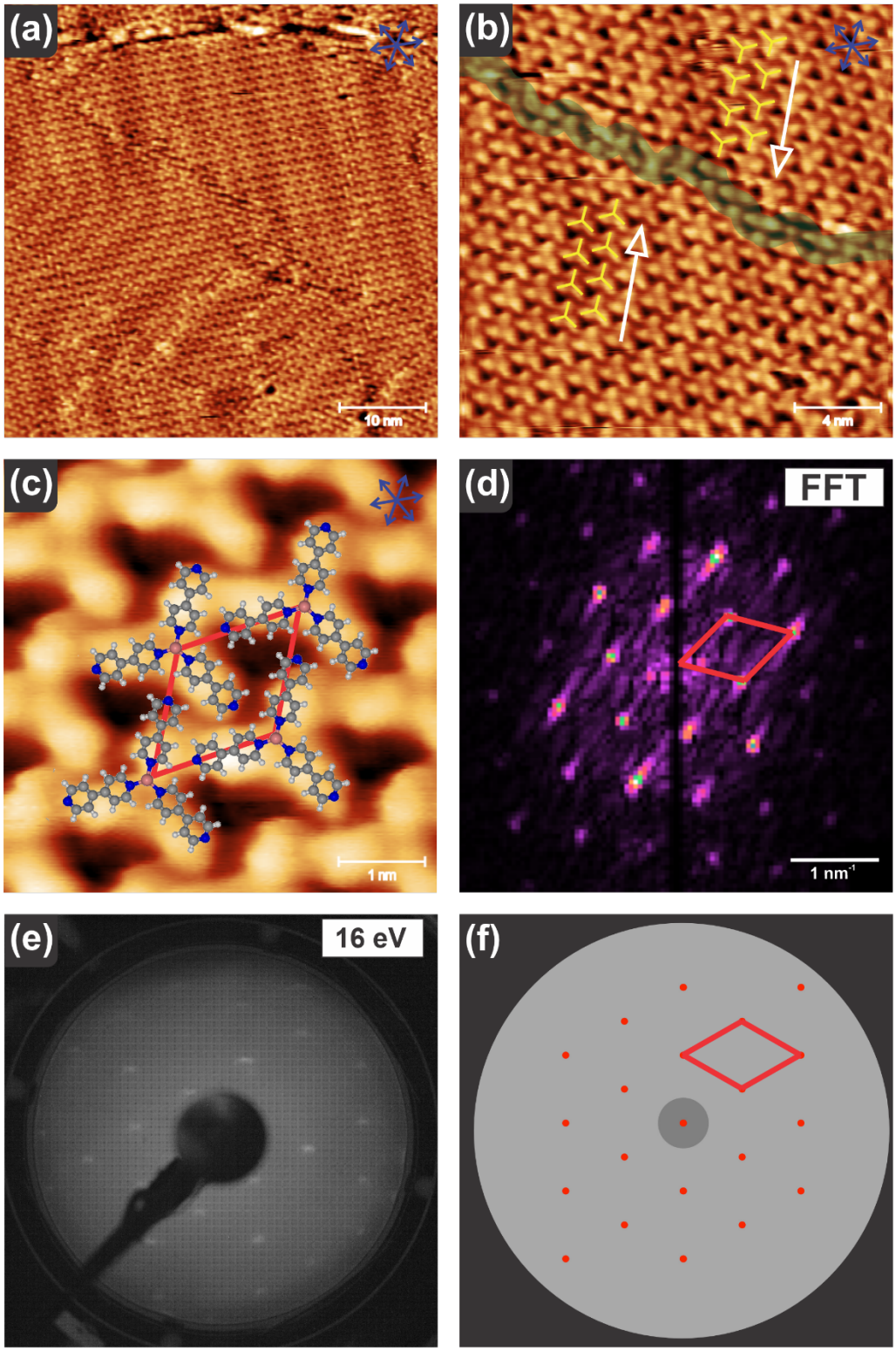

Figure 5. Surface structure after Fe deposition (~0.037 ML, equals ~0.51 Fe/nm^2) onto a saturated 4,4-bipy monolayer on Au(111) at RT, and cooling down to ~105 K. (**a**–**c**) STM images with sizes of 50 nm × 50 nm, 10 nm × 10 nm, and 5 nm × 5 nm, respectively, displaying a well-ordered hexagonal lattice of triangular protrusions, which are assigned to tripods formed by three molecules coordinated by a central Fe atom (reddish dot). The Au(111) substrate directions are indicated by blue arrows in the top right corners. In (**b**) two domains with different orientation of the tripods are present (indicated by yellow tripods bars and white arrows); the corresponding domain boundary is marked in green. In (**c**), the real space unit cell is shown as red square, and the scaled DFT-derived structure of a free-standing layer with 0° rotation of the tripods (see text) is superimposed. (**d**) FFT of the STM image. (**e**) LEED pattern measured with a beam energy of 16 eV. (**f**) Schematic LEED pattern. In (**d**–**f**), the reciprocal unit cell is indicated as red square. For measurement parameters, please refer to the SM (Table S3).

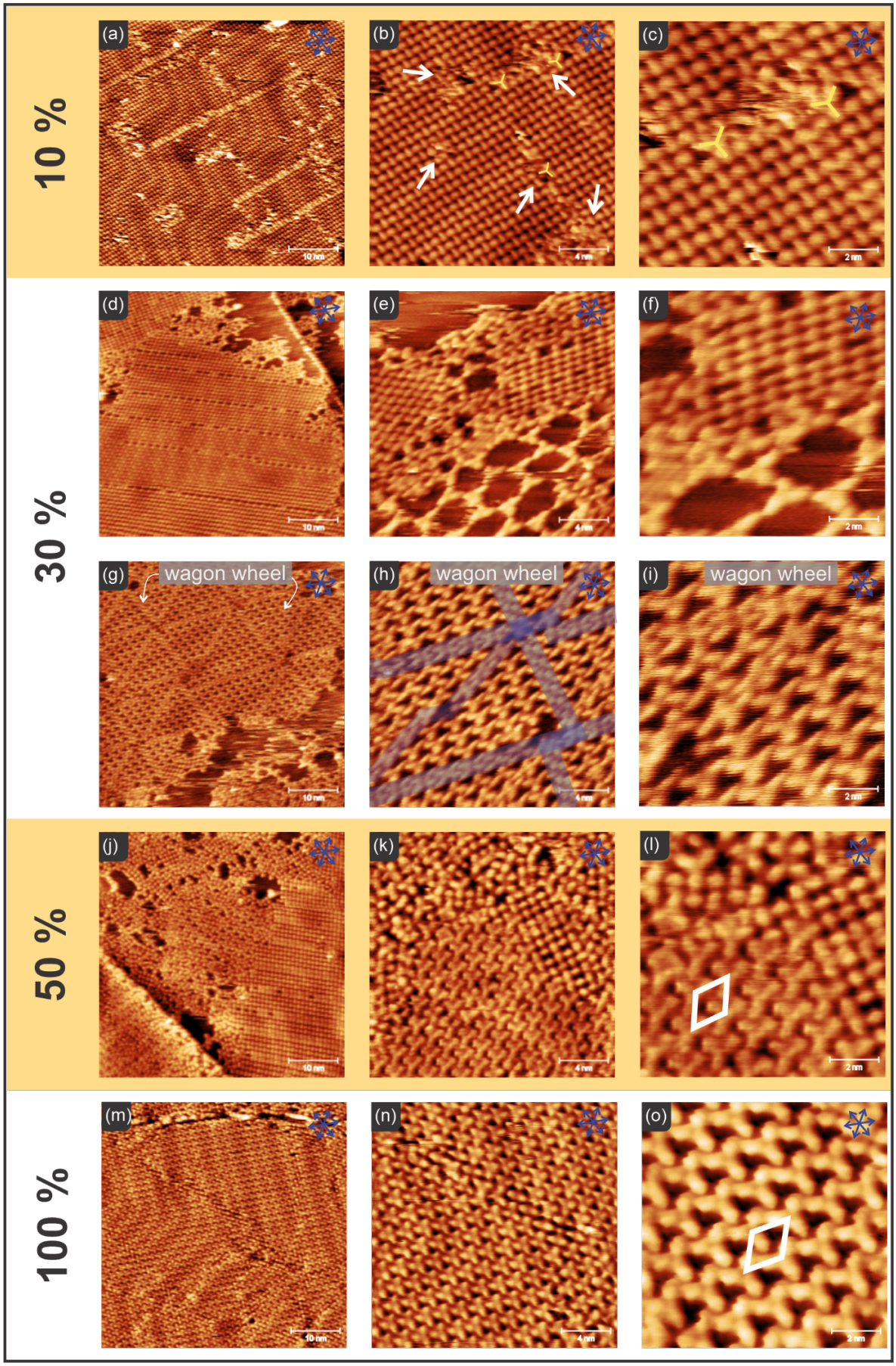

Figure 6. STM images of a 4,4-bipy monolayer after adding different doses of Fe at RT. An Fe dose of 100% (**m**–**o**) equals ~0.037 ML or ~0.51 Fe/nm^2 (300 sec Fe evaporation, I_{flux} = 1.0 nA). The image sizes decrease (left to right) from 50 nm × 50 nm to 20 nm × 20 nm, and 10 nm × 10 nm. (**a**–**c**) 10% (30 sec Fe): Fe-induced defect sites are marked with white arrows, first tripods with yellow tripod bars. (**d**–**i**) 30% (90 sec Fe): the upper panel shows a

region with disordered tripods at the edges of the T-shape structure, and tripods partially arranging in a pore-like orientation (note that these pores are different from the hexagonal pores in Figure 4); the lower panel shows a region of tripods in a wagon wheel structure, with mirror twin boundaries marked in blue (**h**). (**j**–**l**) 50% (150 sec Fe): Coexistence of ordered tripod and T- shape structures, and disordered tripods (k, top left). The tripod unit cell is marked in white. (**m**–**l**) 100% Fe dose (see above). The tripod unit cell is marked in white. Images (**a**–**l**) were recorded on one sample by successively adding Fe, while (**m**–**o**) were recorded on different samples. The Au(111) substrate directions are indicated by blue arrows in the top right corners. A larger data set with additional Fe doses equal of 70% and 90% is shown in the SM (Figure S8). All images were recorded at ~105 K. For measurement parameters, please refer to the SM (Table S3).

Upon increasing the Fe dose to 30%, we find the coexistence of the T-shape structure and tripods: Disordered tripods are observed at the edges of the T-shape islands, and some of the tripods are arranged in a pore-like manner (Figure 6d). Some areas on the surface already show the formation of larger tripod arrangements (Figure 6e,f), and occasionally islands with tripods arranged in a wagon wheel structure were found (Figure 6g–i). This wagon wheel structure displays mirror twin boundaries (shaded in blue in Figure 6h) that are formed during the growth process. A similar pattern has been reported for e.g., the self-assembly of 2,3-diaminophenazine on $MoSe_2$ [26].

Increasing the Fe dose further (50%) progresses the process of tripod formation, and the STM images show the coexistence of ordered tripods and T-shape structures; see Figure 6j–l). The tripod structure unit cells are marked with white parallelograms. No more wagon wheel pattern was found. As we can only probe a small fraction of the surface, a determination of a tripod/T-shape ratio was not possible, and we also cannot exclude areas with wagon wheel patterns on the surface. The dose was further increased to 70% and 90% and again coexisting tripod and T-shape structures were observed; these data are shown in Figure S8 in the SM. Figure 6m–o shows again the full tripod layer after a Fe dose of 100% for comparison.

Finally, we annealed a full tripod-covered surface to 400 K for 10 min (note that similar effects are already observed for annealing starting at 340 K). Figure 7 shows that this heating step leads to a significant decrease of the surface coverage (similar to Figure 2), which we attribute to desorption of 4,4-bipy after desintegration of a certain fraction of the tripods, since ordered tripod regions have disappeared from the surface. Instead of tripod islands, we observe the coexistence of islands consisting of hexagonal pores (indicated by red dots in Figure 7a) and T-shape islands (indicated with white dots). Both structures can connect through single 4,4-bipy arms of a tripod (Figure 7b, yellow tripod) interacting with terminating 4,4-bipy molecules on the edges of the T-shape island (indicated as green bars). In addition, tripods arranged in chains are observed (indicated by white arrows). These chains are composed of intact tripods, where each 4,4-bipy molecule is coordinated to one Fe-atom, but also of 4,4-bipy molecules coordinated to two Fe atoms. The required additional Fe atoms stem from the desintegration of tripods, yielding three 4,4-bipy molecules per Fe atom, which then form the observed T-shape islands or desorb. The chains are thus considered as a transition structure toward the hexagonal pore structure, where each 4,4-bipy molecule is coordinated to two Fe atoms (see below). On a closer look at the chains, we observe that the protrusion in the position of the 4,4-bipy arm facing perpendicular to the chain directions, that is, the single-coordinated 4,4-bipy molecules, appears broader than the protrusions in the direction of the chain (Figure 7c), that is, the doubly-coordinated 4,4-bipy molecules. This observation indicates some mobility of this 4,4-bipy arm (blue arrows). Also, shifts in the image during the scan (yellow arrows) indicate the mobility of single 4,4-bipy molecules.

Some surface areas even show extended periodic pore structures, as shown in Figure 8 (and Figure S3 in the SM) for a separately prepared sample. Notably, we have chosen a region on the surface where only the pore structure is seen, while on other regions the coexisting T-shape structure can be found, similar to Figure 7. This structure represents a 2D MOF with a regular hexagonal Kagome pattern [27], which is marked with a turquoise star in Figure 8a. The electronic and magnetic behavior of Kagome lattices on different substrates have been extensively studied [28–33]. However, as these properties are not the focus of our present work, we refrain from addressing them here. In Figure 8c, we have superimposed a scaled model of the Kagome pores, where hexagonally arranged Fe centers (reddish dots) are connected by single 4,4-bipy molecules through coordination to the N-atom of the pyridine rings on both sides (Figure 8c). This results in a hexagonal unit cell with unit cell vectors of equal length of 2.00 ± 0.15 nm. The corresponding FFT, along with the unit cell in reciprocal space, is displayed in Figure 8d.

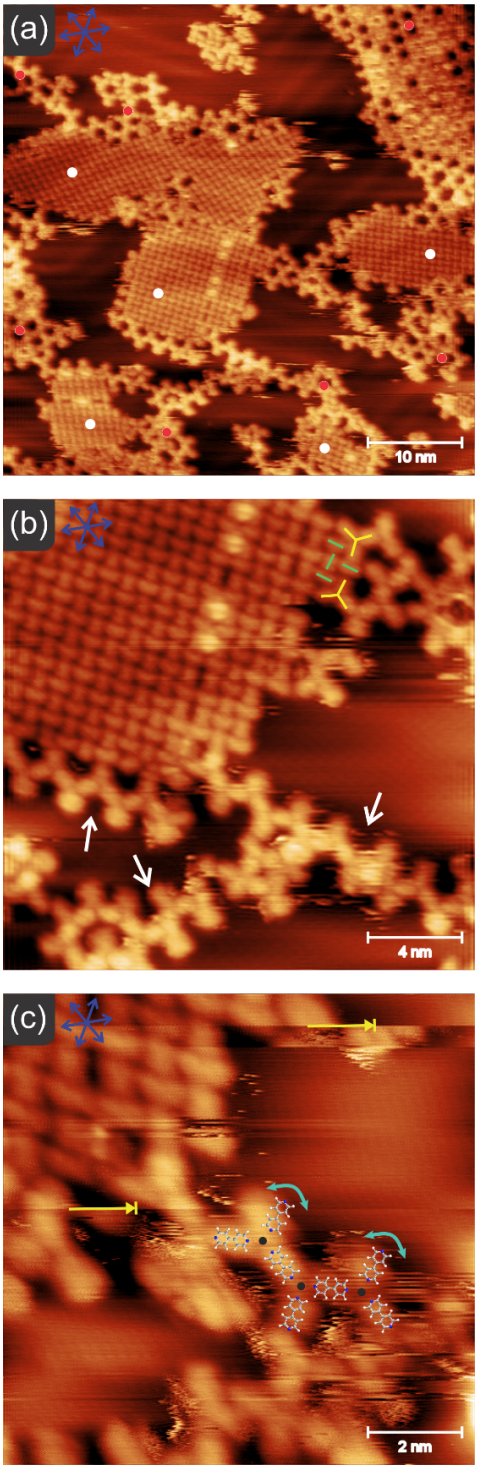

Figure 7. STM images obtained after annealing an extended tripod layer (equal to 100% in Figure 6) to 400 K for 10 min, which yielded an overall decrease of surface coverage; images were recorded at ~105 K. (**a**) 50 nm × 50 nm, (**b**) 20 nm × 20 nm, (**c**) 10 nm × 10 nm). The surface is covered by T-shape islands (white dots) and hexagonal pores (red dots). (**b**) shows a zoom-in at the edge of a T-shape island. Tripod chains are marked with white arrows. At the edges of the T-shape islands, uncoordinated 4,4-bipy molecules of the T-shape structure interact with the coordinated three-fold Fe coordinated structures (e.g., tripods, chains). This interaction is marked exemplary by green bars for the uncoordinated molecules and yellow tripod bars for the three-fold coordinated units. (**c**) shows a zoom-in on the chain structure. Mobile species (possibly tip-induced) are marked with yellow arrows. A scaled model for the chain structure is placed on the chain. Black dots mark the position of the Fe coordination center. Protrusion facing perpendicular to the chain direction appears broader (scaled molecule does also not fit in that position). This is due to the mobility of the 4,4-bipy arm. The mobility id marked by turquoise arrows. Surface crystal directions are marked with dark blue arrow next to the image label. For measurement parameters, please refer to the SM (Table S3).

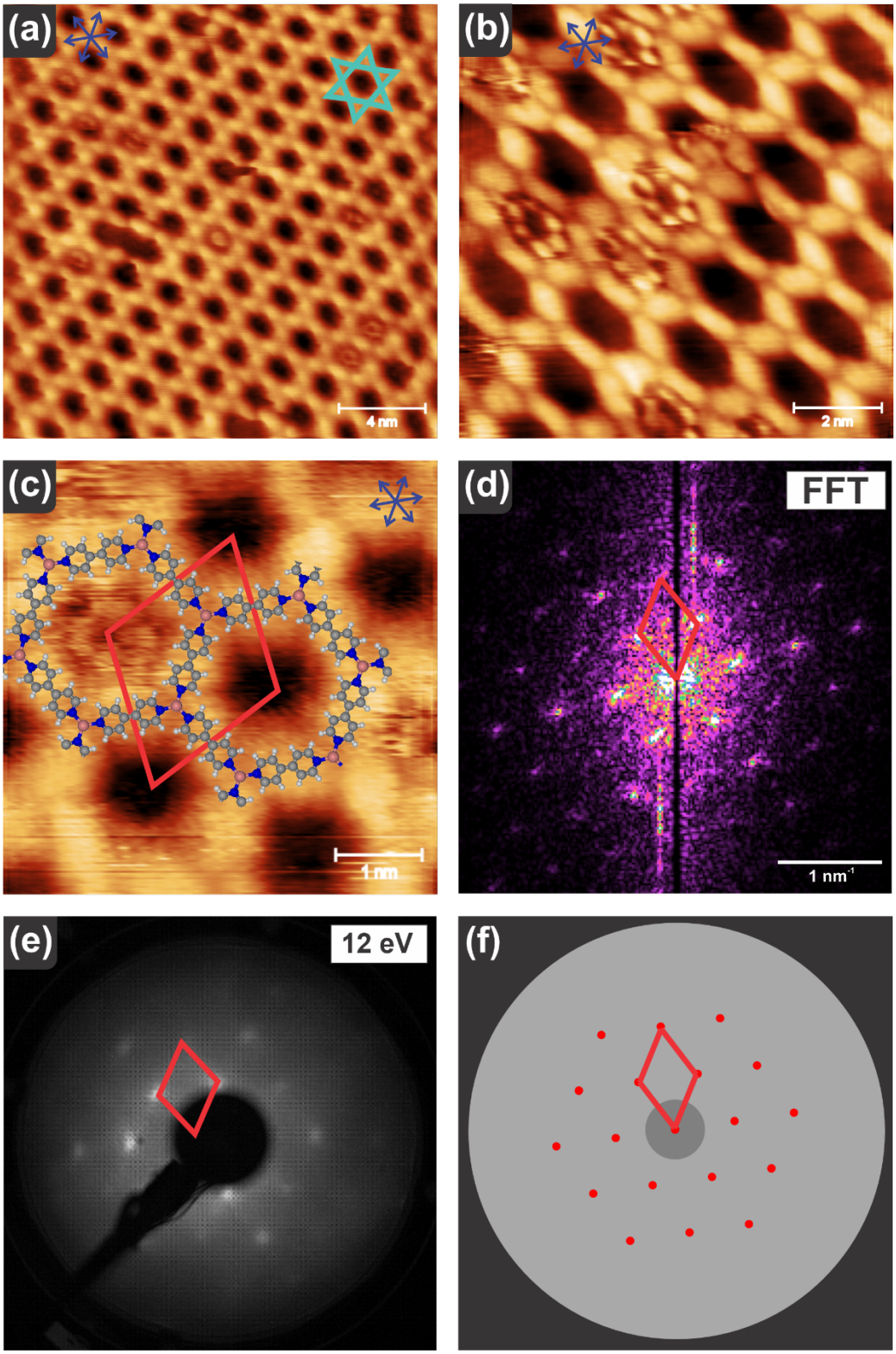

Figure 8. STM images of the pore structure (Kagome lattice), obtained after annealing an extended tripod layer (equal to 100% in Figure 6) to 400 K for 10 min (same as in Figure 7), which yielded an overall decrease of surface coverage; images were recorded at ~105 K, in a region of local high surface coverage displaying only the pore structure. (**a**–**c**) STM measurements with image sizes of 20 nm × 20 nm, 10 nm × 10 nm, and 5 nm × 5 nm, respectively. The Au(111) substrate directions are indicated by blue arrows in the top left corners. In (**a**), the Kagome lattice that is marked by a turquoise star. In (**c**), the real space unit cell is shown as red square, and the scaled structure calculated by DFT for a free-standing layer (see text) is superimposed with reddish dots indicating the position of the Fe coordination center. (**d**) FFT of the STM image. (**e**) LEED pattern measured with a beam energy of 12 eV. (**f**) Schematic LEED pattern. In (**d**–**f**), the reciprocal unit cell is indicated as red square. For measurement parameters, please refer to the SM (Table S3).

In some cases, we could even obtain a well-defined hexagonal LEED pattern of the Kagome structure. An example is shown in Figure 8e (beam energy: 12 eV), along with the corresponding schematic pattern in Figure 8f, and in line with the FFT image. The reciprocal unit cell is shown in red in Figure 8d–f.

We also performed DFT calculations of a free-standing pore structure (again neglecting the interaction with the substrate), in order to obtain some understanding on the energetics of the pore formation (see Figure S9a in the SM). The hexagonal structure is planar and has a lattice constant of 1.94 nm, which agrees very well with the value of 2.00 ± 0.15 nm determined from STM. The calculated structure is superimposed on the STM image in Figure 8c. The formation energy of the hexagonal pattern is 7.84 eV per unit cell (three 4,4-bipyridine and two Fe atoms) and 2.61 eV per molecule; thus, the structure is thermodynamically very stable (see Table S1 in the SM).

Inspection of the STM image in Figure 8 reveals that some of the pores are filled, Figure 8b. In some cases, the filling appears as six small protrusions or as a small ring inside the pore frame structure. We cannot unequivocally identify the species in the pore. However, since the pore is too small for six 4,4-bipy molecules, we speculate that the protrusions are due to one or several mobile molecules statistically adsorbed or rotating in the pore. Similar observations have been made for other systems [34,35].

3. Summary and Conclusions

We observe coverage-dependent phase transformations of 4,4-bipy and Fe on Au(111), from pure phases to a surface MOF (2D MOF). Figure 9 shows an overview of the observed long-range-ordered periodic structures: (a) The T-shape structure TS, formed by the 4,4-bipy molecules without an Fe coordination; (b) the tripod structure T, formed by Fe centers (reddish dots) three-fold coordinated to 4,4-bipy via the N-atom of one pyridine group; (c) the Kagome pore K, which is a 2D MOF formed by hexagonally arranged Fe centers three-fold coordinated to 4,4-bipy molecules through the N-atoms of both pyridine rings. The unit cells are marked in red. The unit cell parameters, the number of 4,4-bipy molecules (M) and Fe atoms per unit cell (in red), and the densities of 4,4-bipy (ρ_M) and Fe atoms (ρ_{Fe}) are given on the bottom for each structure.

Considering all structures, we find that the transformation between the structures depends solely on the availability of 4,4-bipy molecules (M), Fe atoms (Fe) and free surface area (Figure 10). Upon annealing, a full layer of tripods transforms into T-shape islands and Kagome pores (T → K + TS), with partial desorption of 4,4-bipy molecules. Considering the number of 4,4-bipy and Fe per unit cell for each structure, we can formulate the following reaction equation:

$$2 \times (3\mathrm{M}\ 1\mathrm{Fe}) \leftrightarrow (3\mathrm{M}\ 2\mathrm{Fe}) + 3\mathrm{M}$$

This equation shows that the formation of one Kagome pore (3M 2Fe) requires two tripods (3M 1Fe), leaving an excess of three 4,4-bipy molecules (M). These excess molecules then form the T-shape structure (see Figure 7) or desorb. The M and Fe amounts of the different structures (unit cells) show clearly why a direct transformation from a full layer of tripods to only Kagome pores is not possible, and why a T-shape phase has to be formed together with the Kagome phase. The T-shape islands are not Fe-coordinated (and can/will desorb, depending on temperature). Adding more Fe to this system transforms the remaining T-shape islands into Kagome pores (TS → K) without an additional annealing step. Additionally, the overall coverage decreases. This indicates that the annealing step is only required to partially desorb the 4,4-bipy in order to create space for the Kagome pores, but not for the formation of the pore itself. Adding more 4,4-bipy to the Kagome pores transforms the pores back to the tripod structure (K → T), as a denser packing is required to incorporate the additional molecules. In the case of the Kagome pores coexisting with the T-shape structure, we also find a transformation to the tripods with additional 4,4-bipy dosing (K + TS → T), but we cannot exclude remaining T-shape islands, as the formation of tripods from T-shape arrangements also depends on the availability of Fe on the surface. All three structures are formed with different Fe/4,4-bipy ratios (T-shape: 0/2, Tripods: 1/3, Kagome: 2/3), presenting different molecular densities on the substrate surface, but are all stable at RT. Reversible change between the structures is achieved only by providing or removing Fe or 4,4-bipy. The high arrangement reversibility is possible due to the weak molecule-substrate interactions.

A detailed theoretical exploration of the mechanism of the reversible transformation between the tripod structure and the Kagome structure is out of the scope of the present study, since it would need the explicit inclusion of the Au(111) surface and molecular dynamics simulations. However, analyzing the geometries and energetics of both structures, which both contain three molecules per unit cell, does provide some insight. One the one hand, the formation energy per 4,4-bipy molecule of the Kagome structure is larger than that of the tripod structure by a factor of 1.79 (2.613 vs. 1.460 eV—see Table S1). On the other hand, the 4,4-bipy density in the tripod structure is by a factor of 1.78 larger for the tripod structure (1.54 vs. 0.87 molecules/nm^2—see Figure 9). Thus, these two

effects nearly cancel out, which makes the easy reversible transformation of the two structures by changing the 4,4-bipy coverage understandable.

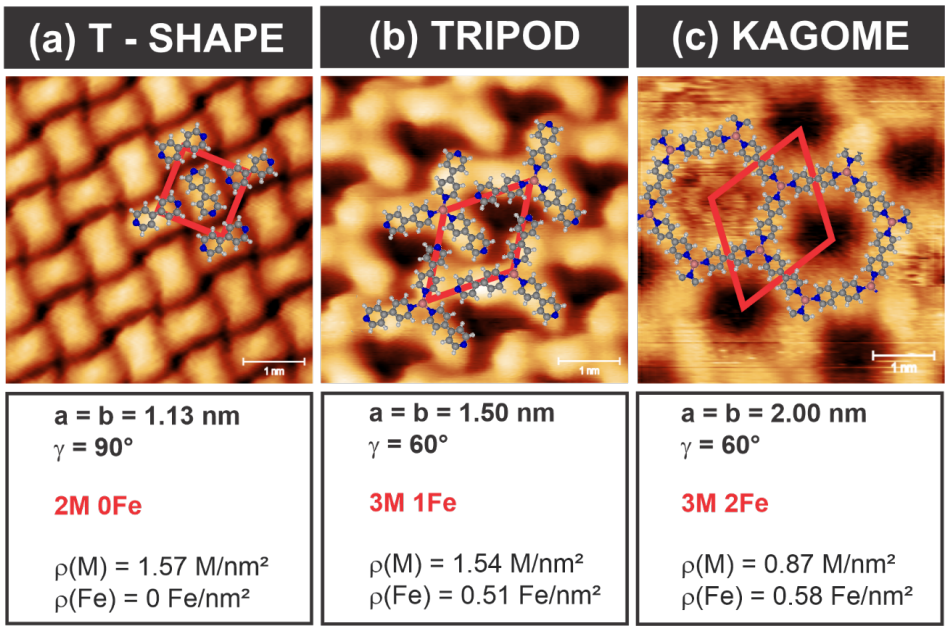

Figure 9. Overview of the STM images (5 nm× 5 nm): (**a**) T-shape structure; (**b**) tripod structure; (**c**) Kagome pores; the unit cells are indicated in red. (Bottom) Structural parameters of the observed periodic structures. a: length of the unit cell vectors; γ: angle of the unit cell; M and Fe: number of the 4,4-bipy molecules and Fe atoms, respectively, per unit cell (in red), ρ(M) and ρ(Fe): density of the 4,4-bipy molecules and Fe atoms, respectively. For measurement parameters, please refer to the SM (Table S3).

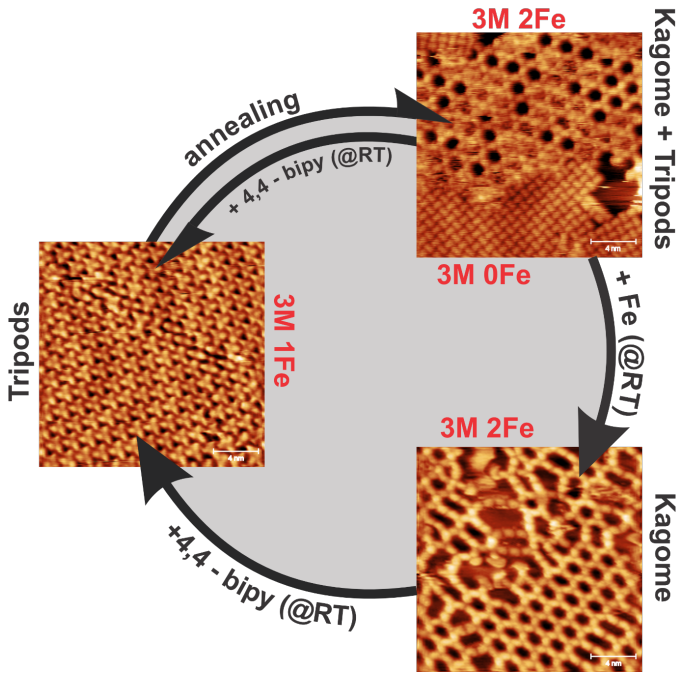

Figure 10. Schematic illustration with exemplary STM images (20 nm × 20 nm) of the observed phase transformation. After annealing a surface covered with an ordered tripod structure to 340–400 K for 10 min, we observe the transformation to a Kagome pore and T-shape structures (T → K+TS). Note that this process is accompanied by an overall loss in surface coverage, which creates space for the pore formation. Adding more Fe to this system at RT transforms the remaining T-shape structure into Kagome pores (TS → K). No additional heating is required, as the previous annealing step created the required surface area for the Kagome pores. Both the mixed (Kagome + T-shape) and the pure Kagome structures transform back to the ordered Tripod layer when more 4,4-bipy is added to the system (K+TS → T and K → T, respectively). For each structure, the ratio of 4,4-bipy molecules (M) to Fe atoms is given in red. For measurement parameters, please refer to the SM (Table S3).

4. Experimental

All STM and AFM experiments were performed in the constant current mode in a two chamber Scienta Omicron VT-AFM-Q+-Xa instrument. The base pressure of the UHV system was $<1.0 \times 10^{-10}$ mbar. The STM images were recorded using a W-tip at bias voltages −0.8 to −1.4 V (applied to the tip). The nc-AFM images were obtained in non-contact mode with silicon cantilevers, and the applied frequency shifts Δf in the employed experimental conditions ranged from −500 to −600 Hz vs. the cantilever's resonance frequency, which is typically around 270 to 300 kHz. A bias voltage of −0.60 V to −1.4 V was applied to the AFM tip for better resolution. The Au(111) crystal was obtained from MaTeck and cleaned via cycles of Ar^+ ion sputtering and annealing to ~900 K. The 4,4-bipyridine was purchased from Sigma-Aldrich Co. (Grade: 98%). 4,4-bipy was deposited using a home-built, water-cooled effusion cell. The effusion cell can be separated from the main chamber with a gate valve and it can be separately pumped via a turbopump (with a second gate valve). Thus, it can be refilled without breaking the vacuum in the main chamber. Due to its high vapor pressure, 4,4-bipy evaporates under UHV conditions at RT. When the effusion cell was not used, both valves are closed and an equilibrium vapor pressure builds up in the effusion cell chamber. For dosing, the valve to the turbo pump was opened for a short time (10 s) to pump out 4,4-bipy and possible contamination from the effusion cell chamber. Thereafter, the valve to the main chamber was opened, and the evaporating 4,4-bipy was dosed onto the sample via resulting the chamber background pressure of 4.0×10^{-5} for 5 min. While the evaporator was typically at RT, at low evaporator filling mild heating was necessary to increase the vapor pressure. While this procedure allowed us to prepare well-defined and clean (as judged from STM) 4,4-bipy layers, controlling the exact dose was a challenge. After dosing, the samples were left at RT overnight after 4,4-bipy evaporation to desorb second layer species.

Fe was evaporated using a 3-fold metal evaporator from Specs using a flux current of 1.0 nA. During 4,4-bipy and Fe evaporation the sample was always at RT (~ 300 K). The samples were cooled down to ~105 K for the STM and nc-AFM measurements. The STM images were processed using the Gwyddion software [36]. Each image was background subtracted and moderately 2D filtered. The unit cells were determined using the Gwyddion "measure lattice" feature and by measuring distances in the WSxM [37] software. A drift correction according to Rahe et al. [38] was applied to selected images using the Corel Draw software. The LEED images were recorded using a 4-grid SPECTALEED from Scienta Omicron with a LaB_6 Filament. The LEED pattern simulations were obtained using the ProLEED software [39].

Supplementary Materials

The additional data and information can be downloaded at: https://media.sciltp.com/articles/others/2605251129021180/AC-26030207-SM.pdf. Figure S1. Saturated 4,4-bipy monolayer on Au(111), deposited at RT and cooled down to ~105 K for the measurements. Comparison of STM (a,b) and nc-AFM (c,d) images with sizes of 50 nm × 50 nm (top) and 20 nm × 20 nm (bottom), displaying a well-ordered quadratic lattice with two perpendicularly oriented molecules in a T-shape arrangement per unit cell; for details see manuscript. The STM data are from the same sample as those in Figure 1 in the manuscript. Measurement parameters are provided in Table S3. Figure S2. Tripod structure on Au(111), obtained after Fe deposition (~0.037 ML, equals ~0.51 Fe/nm^2) onto a saturated 4,4-bipy monolayer on Au(111) at RT, and cooling down to ~105 K. Comparison of STM (a,b) and nc-AFM (c,d) images with sizes of 50 nm × 50 nm (top) and 20 nm × 10 nm (bottom), displaying a well-ordered hexagonal lattice of triangular protrusions, which are assigned to tripods formed by three molecules coordinated by a central Fe atom; for details see manuscript. The STM data are from the sample as those in Figure 5 in the manuscript. Measurement parameters are provided in Table S3. Figure S3. Hexagonal pore structure (Kagome lattice) on Au(111), obtained after annealing an extended tripod layer to 400 K for 10 min and cooling down to ~105 K, in a region of local high surface coverage displaying only the pore structure. Comparison of STM (a,b) and nc-AFM (c,d) images with sizes of 50 nm × 50 nm (top) and 20 nm × 20 nm (bottom); for details see manuscript. The STM data are from the same sample as those in Figure 8 in the manuscript. Measurement parameters are provided in Table S3. Figure S4. Exemplary STM images (left: 50 nm × 50 nm, right: 20 nm × 20 nm) showing coexisting domains with different orientations of the T-shape structure formed by 4,4-bipy on Au(111). The Au(111) substrate directions are indicated by blue arrows in the top right corners. Measurement parameters are provided in Table S3. Figure S5. LEED patterns recorded of a saturated 4,4-bipy film on Au(111) arranged in a T-shape pattern at different beam energies (given in top right corner of each image). Figure S6. LEED pattern of a T-shape 4,4-bipy monolayer on Au(111) recorded at a beam energy of 17 eV (left). Simulated LEED pattern in shown on the right. TOP: Quadratic pattern of one domain is marked by a red grid in both the LEED and the simulated pattern. Reflexes are numbered in the grid for the simulated pattern (XY). Due to the mirror glide plane symmetry of the T-shape structure the 10 and 01 diffraction spots are not visible. Therefore, all spots on the green circle are not seen in the diffraction pattern. A total of 6 domains gives then the resulting diffraction pattern shown again for comparison (bottom) A single exemplary unit cell is marked with a red square in both the LEED (left) and simulated pattern (right). Figure S7. LEED pattern of the clean Au(111) recorded at a beam energy of 50 eV. The herringbone reconstruction leads to a

splitting of the spots. Notably, at this beam energy the adsorbate superstructure spots are too weak to be seen. Figure S8. STM images of a 4,4-bipy monolayer after adding different doses of Fe at RT. An Fe dose of 100% (m–o; 300 sec Fe evaporation, I_{flux} = 1.0 nA) equals ~0.037 ML or ~0.51 Fe/nm^2. The image sizes decrease (left to right) from 50 nm × 50 nm to 20 nm × 20 nm, and 10 nm × 10 nm. (a–c) 10% (30 s Fe): Fe-induced defect sites are marked with white arrows, first tripods with yellow tripod bars. (d–i) 30% (90 sec Fe): the upper panel shows a region with disordered tripods at the edges of the T-shape structure, and tripods partially arranging in a pore-like orientation (note that these pores are different from the hexagonal pores in Figure 4); the lower panel shows a region of tripods in a wagon wheel structure, with mirror twin boundaries marked in blue (h). (j–l) 50% (150 s Fe): Coexistence of ordered tripod and T-shape structures, and disordered tripods (k, top left). The tripod unit cell is marked in white. (u–w) 70% (210 s Fe): overall very similar to 50%. (x-z) 90% (270 s Fe): already very similar to 100%. (m–l) 100% Fe dose (see above). The tripod unit cell is marked in white. Images (a–l) were recorded on one sample by successively adding Fe, while (m–o) were recorded on different samples. The Au(111) substrate directions are indicated by blue arrows in the top right corners. All images were recorded at ~105 K. For measurement parameters, please refer to Table S3. Figure S9. Optimized geometries of the (a) hexagonal pattern; (b) the tripod pattern with a rotation angle of 0°; and (c) the square pattern. Figure S10. Optimized geometry of the long-pore pattern. Shown are the geometries of (a) the empty pore and (b) the pore filled with three 4,4-bipyridine molecules. Views from the lower edge of the unit cell along the y axis are shown in (c) (perspective parallel to the x-y plane) and (d) (perspective 20° towards the x-y plane). Views from the left edge of the unit cell along the x axis are shown in (e) (perspective parallel to the x-y plane) and (f) (perspective 20° towards the x-y plane). Figure S11. Optimized geometry of the long-pore pattern. Shown are the geometries of (a) the empty pore and (b) the pore filled with twelve 4,4-bipyridine molecules (b). Views from the lower edge of the unit cell along the y axis are shown in (c) (perspective parallel to the x-y plane) and (d) (perspective 20° towards the x-y plane). Views from the left edge of the unit cell along the x axis are shown in (e) (perspective parallel to the x-y plane) and (f) (perspective 20° towards the x-y plane). Table S1. Absolute and relative DFT energies of the optimized structures. The per molecule energies always refer to the relative formation energies of the structures per 4,4-bipyridine units, irrespective of the number of Fe atoms in the structures. Table S2. Absolute and relative energies of the tripod structure for different rotations of the tripods with respect to the unit cell. The unit cell shapes were open for optimization as well, but led to geometries very close to hexagonal in all cases. The systems are named according to the initial rotation angles of the tripods. Table S3. Preparation and measurement details of shown STM images. T_{evap}: temperature of the sample during the 4,4-bipy evaporation, T_{max}: highest temperature the sample has experienced during the time of the scan (indicated the last annealing process), T_{meas}: temperature at which the image was recorded. For STM, the tunneling current (I_T), and for AFM, the frequency shift (Df) is given. For images not labeled as (a), (b), (c), etc. the following identification markers are used: t = top, m= middle, b = bottom, r = right, l = left. Post-measurement corrections such as drift correction or cutting of the originally measured STM image are labeled in the "Note-column". References [40–45] are cited in supplementary materials.

Author Contributions

A.G.: investigation (experiments), writing—original draft, validation, visualization, methodology, formal analysis, data curation; S.S.: investigation (experiments), visualization, methodology, formal analysis; J.S.: investigation (theory), conceptualization, writing—original draft, visualization, methodology, formal analysis, software, data curation; A.C.: conceptualization, validation, writing—review & editing; I.T.: investigation (experiments); N.W.-W.: investigation (experiments); A.d.S.: conceptualization writing—review & editing, supervision, project administration, funding acquisition; H.-P.S.: conceptualization writing—review & editing, validation, supervision, project administration, funding acquisition, data curation. All authors have read and agreed to the published version of the manuscript.

Funding

The authors gratefully acknowledge funding by the German Research Foundation (DFG) through RTG 2861 (Project Number 491865171) at the Friedrich-Alexander-Universität Erlangen-Nürnberg (FAU) and the TU Dresden, and by the German Academic Exchange Service (DAAD) through Project PPP 57705724 at FAU. The Brazilian authors gratefully acknowledge funding by Coordination for the Improvement of Higher Education Personnel (CAPES) through project PROBRAL 627947/2021, and the São Paulo Research Foundation (FAPESP) through Project 2022/12929-3. The authors further gratefully acknowledge the scientific support and HPC resources provided by the Erlangen National High Performance Computing Center (NHR@FAU) of FAU under the NHR Project b146dc. NHR funding is provided by federal and Bavarian state authorities. NHR@FAU hardware is partially funded by the German Research Foundation (DFG; Project Number 440719683). AC thanks the Alexander von Humboldt Foundation for a research fellowship.

Institutional Review Board Statement

Not applicable.

Informed Consent Statement

Not applicable.

Data Availability Statement

The source data used in this paper will be available on Zenodo upon publication: https://zenodo.org/uploads/19236673.

Conflicts of Interest

The authors declare no conflict of interest.

Use of AI and AI-Assisted Technologies

No AI tools were utilized for this paper.

References

1. Chakraborty, G.; Park, I.-H.; Medishetty, R.; et al. Two-Dimensional Metal–Organic Framework Materials: Synthesis, Structures, Properties and Applications. *Chem. Rev.* **2021**, *121*, 3751–3891. https://doi.org/10.1021/acs.chemrev.0c01049.
2. Lee, M.K.; Shokouhimehr, M.; Kim, S.Y.; et al. Two-Dimensional Metal–Organic Frameworks and Covalent–Organic Frameworks for Electrocatalysis: Distinct Merits by the Reduced Dimension. *Adv. Energy Mater.* **2022**, *12*, 2003990. https://doi.org/10.1002/aenm.202003990.
3. Liu, J.; Xing, G.; Chen, L. 2D Conjugated Metal–Organic Frameworks: Defined Synthesis and Tailor-Made Functions. *Acc. Chem. Res.* **2024**, *57*, 1032–1045. https://doi.org/10.1021/acs.accounts.3c00788.
4. Furukawa, H.; Cordova, K.E.; O'Keeffe, M.; et al. The Chemistry and Applications of Metal-Organic Frameworks. *Science* **2013**, *341*, 1230444. https://doi.org/10.1126/science.1230444.
5. Cadiau, A.; Adil, K.; Bhatt, P.M.; et al. A Metal–Organic Framework–Based Splitter for Separating Propylene from Propane. *Science* **2016**, *353*, 137–140. https://doi.org/10.1126/science.aaf6323.
6. Kim, E.J.; Siegelman, R.L.; Jiang, H.Z.H.; et al. Cooperative Carbon Capture and Steam Regeneration with Tetraamine-Appended Metal–Organic Frameworks. *Science* **2020**, *369*, 392–396. https://doi.org/10.1126/science.abb3976.
7. Bavykina, A.; Kolobov, N.; Khan, I.S.; et al. Metal–Organic Frameworks in Heterogeneous Catalysis: Recent Progress, New Trends, and Future Perspectives. *Chem. Rev.* **2020**, *120*, 8468–8535. https://doi.org/10.1021/acs.chemrev.9b00685.
8. Lin, Z.-J.; Lü, J.; Hong, M.; et al. Metal–Organic Frameworks Based on Flexible Ligands (FL-MOFs): Structures and Applications. *Chem. Soc. Rev.* **2014**, *43*, 5867–5895. https://doi.org/10.1039/C3CS60483G.
9. Mínguez Espallargas, G.; Coronado, E. Magnetic Functionalities in MOFs: From the Framework to the Pore. *Chem. Soc. Rev.* **2018**, *47*, 533–557. https://doi.org/10.1039/C7CS00653E.
10. Deng, H.; Grunder, S.; Cordova, K.E.; et al. Large-Pore Apertures in a Series of Metal-Organic Frameworks. *Science* **2012**, *336*, 1018–1023. https://doi.org/10.1126/science.1220131.
11. Férey, G.; Serre, C. Large Breathing Effects in Three-Dimensional Porous Hybrid Matter: Facts, Analyses, Rules and Consequences. *Chem. Soc. Rev.* **2009**, *38*, 1380–1399. https://doi.org/10.1039/B804302G.
12. Beurroies, I.; Boulhout, M.; Llewellyn, P.L.; et al. Using Pressure to Provoke the Structural Transition of Metal–Organic Frameworks. *Angew. Chem. Int. Ed.* **2010**, *49*, 7526–7529. https://doi.org/10.1002/anie.201003048.
13. Fernández-Seriñán, P.; Roztocki, K.; Safarifard, V.; et al. Modulation of the Dynamics of a Two-Dimensional Interweaving Metal-Organic Framework through Induced Hydrogen Bonding. *Inorg. Chem.* **2024**, *63*, 5552–5558. https://doi.org/10.1021/acs.inorgchem.3c04522.
14. Shi, Z.; Liu, J.; Lin, T.; et al. Thermodynamics and Selectivity of Two-Dimensional Metallo-Supramolecular Self-Assembly Resolved at Molecular Scale. *J. Am. Chem. Soc.* **2011**, *133*, 6150–6153. https://doi.org/10.1021/ja2010434.
15. Fan, Q.; Liu, L.; Dai, J.; et al. Surface Adatom Mediated Structural Transformation in Bromoarene Monolayers: Precursor Phases in Surface Ullmann Reaction. *ACS Nano* **2018**, *12*, 2267–2274. https://doi.org/10.1021/acsnano.7b06787.
16. Urgel, J.I.; Écija, D.; Lyu, G.; et al. Quasicrystallinity Expressed in Two-Dimensional Coordination Networks. *Nat. Chem.* **2016**, *8*, 657–662. https://doi.org/10.1038/nchem.2507.

17. Lu, J.; Nieckarz, D.; Jiang, H.; et al. Order–Disorder Transition of Two-Dimensional Molecular Networks through a Stoichiometric Design. *ACS Nano* **2023**, *17*, 20194–20202. https://doi.org/10.1021/acsnano.3c05945.
18. Legon, A.C.; Millen, D.J. Angular Geometries and Other Properties of Hydrogen-Bonded Dimers: A Simple Electrostatic Interpretation of the Success of the Electron-Pair Model. *Chem. Soc. Rev.* **1987**, *16*, 467–498. https://doi.org/10.1039/CS9871600467.
19. Jeffrey, G.A. *An Introduction to Hydrogen Bonding*; Oxford University Press: Oxford, UK, 1997.
20. Ireta, J.; Neugebauer, J.; Scheffler, M. On the Accuracy of DFT for Describing Hydrogen Bonds: Dependence on the Bond Directionality. *J. Phys. Chem. A* **2004**, *108*, 5692–5698. https://doi.org/10.1021/jp0377073.
21. Holland, B.W.; Woodruff, D.P. Missing Spots in Low Energy Electron Diffraction. *Surf. Sci.* **1973**, *36*, 488–493. https://doi.org/10.1016/0039-6028(73)90397-X.
22. Yang, W.S.; Jona, F. Missing Spots in Low-Energy Electron-Diffraction Patterns. *Phys. Rev. B* **1984**, *29*, 899–906. https://doi.org/10.1103/PhysRevB.29.899.
23. Dubois, M.; Guillermet, O.; Gauthier, S.; et al. Influence of Cu Adatoms on the Molecular Assembly of 4,4′-Bipyridine on Cu(111). *Phys. Chem. Chem. Phys.* **2018**, *20*, 15350–15357. https://doi.org/10.1039/c8cp01184b.
24. Lin, W.-C.; Chang, H.-Y.; Hu, Y.-C.; et al. Manipulated Nucleation of Fe Nanostructures on Au(111) with Combined Growth Methods. *Nanotechnology* **2010**, *21*, 015606. https://doi.org/10.1088/0957-4484/21/1/015606.
25. Kuliga, J.; Zhang, L.; Lepper, M.; et al. Metalation and Coordination Reactions of 2*H*-*meso*-*trans*-Di(*p*-cyanophenyl)porphyrin on Ag(111) with Coadsorbed Cobalt Atoms. *Phys. Chem. Chem. Phys.* **2018**, *20*, 25062–25068. https://doi.org/10.1039/c8cp05255g.
26. He, X.; Zhang, L.; Chua, R.; et al. Selective Self-Assembly of 2,3-Diaminophenazine Molecules on $MoSe_2$ Mirror Twin Boundaries. *Nat. Commun.* **2019**, *10*, 2847. https://doi.org/10.1038/s41467-019-10801-0.
27. Syôzi, I. Statistics of Kagomé Lattice. *Prog. Theor. Phys.* **1951**, *6*, 306–308. https://doi.org/10.1143/ptp/6.3.306.
28. Hua, M.; Xia, B.; Wang, M.; et al. Highly Degenerate Ground States in a Frustrated Antiferromagnetic Kagome Lattice in a Two-Dimensional Metal–Organic Framework. *J. Phys. Chem. Lett.* **2021**, *12*, 3733–3739. https://doi.org/10.1021/acs.jpclett.1c00598.
29. Farnell, D.J.J. Emergence of Magnetic Order in Kagomé Antiferromagnets. *Front. Phys.* **2019**, *14*, 23302. https://doi.org/10.1007/s11467-019-0886-3.
30. Han, T.-H.; Helton, J.S.; Chu, S.; et al. Fractionalized Excitations in the Spin-Liquid State of a Kagome-Lattice Antiferromagnet. *Nature* **2012**, *492*, 406–410. https://doi.org/10.1038/nature11659.
31. Pati, S.K.; Rao, C.N.R. Kagome Network Compounds and Their Novel Magnetic Properties. *Chem. Commun.* **2008**, *39*, 4683–4693. https://doi.org/10.1039/B807207H.
32. Wang, X.-B.; Xia, B.; Lyu, C.-K.; et al. A *p*-Orbital Honeycomb-Kagome Lattice Realized in a Two-Dimensional Metal-Organic Framework. *Commun. Chem.* **2023**, *6*, 73. https://doi.org/10.1038/s42004-023-00869-7.
33. Ohgushi, K.; Murakami, S.; Nagaosa, N. Spin Anisotropy and Quantum Hall Effect in the Kagomé Lattice: Chiral Spin State Based on a Ferromagnet. *Phys. Rev. B* **2000**, *62*, R6065-R6068. https://doi.org/10.1103/PhysRevB.62.R6065.
34. Carreño-Diaz, V.; Ceccatto, A.; Ferreira, E.; et al. Tailoring Pt-Based Organometallic Porous Network on Ag(111): A Model System for "Host-Guest" Chemistry. *ACS Nanosci. Au* **2026**, *6*, 139–147. https://doi.org/10.1021/acsnanoscienceau.5c00124.
35. Ceccatto, A.; Freiberger, E.M.; Waleska-Wellnhofer, N.J.; et al. Engineering Large Nanoporous Networks with Size and Shape Selected by Appropriate Precursors. *Carbon* **2024**, *221*, 118945. https://doi.org/10.1016/j.carbon.2024.118945.
36. Nečas, D.; Klapetek, P. Gwyddion: An Open-Source Software for SPM Data Analysis. *Open Phys.* **2012**, *10*, 181–188. https://doi.org/10.2478/s11534-011-0096-2.
37. Horcas, I.; Fernández, R.; Gómez-Rodríguez, J.M.; et al. WSXM: A Software for Scanning Probe Microscopy and a Tool for Nanotechnology. *Rev. Sci. Instrum.* **2007**, *78*, 013705. https://doi.org/10.1063/1.2432410.
38. Rahe, P.; Bechstein, R.; Kühnle, A. Vertical and Lateral Drift Corrections of Scanning Probe Microscopy Images. *J. Vac. Sci. Technol. B* **2010**, 28, C4E31–C4E38. https://doi.org/10.1116/1.3360909.
39. Prochazka, P.; Cechal, J. ProLEED Studio: Software for Modeling Low-Energy Electron Diffraction Patterns. *J. Appl. Crystallogr.* **2024**, *57*, 187–193. https://doi.org/10.1107/S1600576723010312.
40. Kresse, G.; Furthmüller, J. Efficient iterative schemes for ab initio total-energy calculations using a plane-wave basis set. *Phys. Rev. B* **1996**, *54*, 11169–11186.
41. Kresse, G.; Furthmüller, J. Efficiency of ab-initio total energy calculations for metals and semiconductors using a plane-wave basis set. *Comput. Mater. Sci.* **1996**, *6*, 15–50.
42. Kresse, G.; Joubert, D. From Ultrasoft Pseudopotentials to the Projector Augmented-Wave Method. *Phys. Rev. B* **1999**, *59*, 1758–1775.
43. Perdew, J.P.; Burke, K.; Ernzerhof, M. Generalized Gradient Approximation Made Simple. *Phys. Rev. Lett.* **1996**, *77*, 3865–3868.

44. Grimme, S.; Antony, J.; Ehrlich, S.; et al. A consistent and accurate ab initio parametrization of density functional dispersion correction (DFT-D) for the 94 elements H-Pu. *J. Chem. Phys*. **2010**, *132*, 154104.
45. Grimme, S.; Ehrlich, S.; Goerigk, L. Effect of the damping function in dispersion corrected density functional theory. *J. Comput. Chem*. **2011**, *32*, 1456–1465.